Size effect on compressive strength of foamed concrete
Experimental and numerical studies

Jiang, Nengdong; Ge, Zhi; Wang, Zhiyuan; Gao, Tianming; Zhang, Hongzhi; Ling, Yifeng; Šavija, Branko

DOI
10.1016/j.matdes.2024.112841

Publication date
2024

Document Version
Final published version

Published in
Materials and Design

Citation (APA)
Jiang, N., Ge, Z., Wang, Z., Gao, T., Zhang, H., Ling, Y., & Šavija, B. (2024). Size effect on compressive strength of foamed concrete: Experimental and numerical studies. *Materials and Design*, *240*, Article 112841. https://doi.org/10.1016/j.matdes.2024.112841

Materials & Design 240 (2024) 112841

Contents lists available at ScienceDirect

Materials & Design

journal homepage: www.elsevier.com/locate/matdes

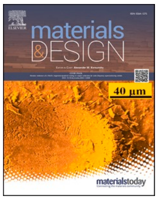

Size effect on compressive strength of foamed concrete: Experimental and numerical studies

Nengdong Jiang [a], Zhi Ge [a,*], Zhiyuan Wang [b], Tianming Gao [a], Hongzhi Zhang [a,*], Yifeng Ling [a], Branko Šavija [c]

[a] School of Qilu Transportation, Shandong University, 250002, Jinan, PR China
[b] Shandong Hi-speed Group 250098, Jian, PR China
[c] Microlab, Faculty of Civil Engineering and Geosciences, Delft University of Technology 2628 CN, Delft, the Netherlands

ARTICLE INFO

Keywords:
Foamed concrete
Lattice model
Compressive strength
Size effect
Lineal-path function

ABSTRACT

This study investigates the size effect on the compressive strength of foamed concrete at the mesoscale level combining X-ray computed tomography (X-CT) and a discrete lattice model. Image segmentation techniques and X-CT were employed to obtain virtual specimens comprising hydrated cement paste and air voids. The lineal-path function and pore size distribution was used to characterise the air void structure. A two-dimensional lattice fracture model of foamed concrete considering different wet densities was established. The model was verified experimentally at a wet density of 700 kg/m^3 and then used to predict the strengths of specimens with wet densities of 600 and 800 kg/m^3. Square and rectangular specimens (slenderness ratio = 2) with widths of 10, 20, 40, 70.7, and 100 mm were investigated. Results show that the air void structure significantly influences the observed size effect on the compressive strength in the investigated size range. A random forest regressor was used to predict the compressive strength of the foamed concrete; the regressor yielded satisfactory results. Finally, existing analytical size effect models were used to fit the simulated strength. Although good fitting was achieved, special attention should be given to the applicable range and physical meaning of fitted empirical parameters.

1. Introduction

Foamed concrete is a lightweight porous construction material into which air bubbles are introduced using a foaming agent [1]. The density of the material can be designed within the range 400–1900 kg/m^3 by precisely controlling the dosage of prefabricated foam [2,3]. Owing to foamed concrete's excellent engineering characteristics, such as low self-weight, high flowability, and adjustable strength, it has been extensively applied to infrastructure construction as non-structural or semi-structural material. For example, foamed concrete has been utilised in tunnel cavity filling [4,5], shock-absorbing barriers for airports [6] and roadbed filling [7].

Understanding the mechanical properties and fracture response of foamed concrete is of practical and scientific significance owing to its extensive application. In practice, compressive strength is the most important mechanical property in construction material design [8]. It has been recognized that the compressive strength is affected by a few parameters, such as density, binder material, water/binder ratio, curing condition and air-void structure [9,10]. Among these factors, binder material and pore structure (including the porosity, diameter, and sphericity of air-voids) are mostly considered. Currently, ordinary Portland cement is the most used binder in foamed concrete [4]. Many scholars have suggested the replacement of a portion of the cement with solid materials to decrease CO_2 emission. It was demonstrated that the replacement of cement with ultra-fine slag [11] and silica fume [12] influence the compressive strength of foam concrete. They can react with the free $Ca(OH)_2$ of hydrated cement to produce calcium–silicate–hydrate, which can improve the compressive strength. In addition, the air void structure is also the major factor affecting the compressive strength of foamed concrete. Guo et al [13] and Zhang et al [14] have established correlations between the compressive strength and pore structure parameters, including pore size distribution, compactness (i.e., uniformity of pore distribution) and sphericity. Nambiar et al. [15] and She et al [16]. have reported that the pore size distribution of foamed concrete with high density is more uniform and narrower than that with low density, which is attributed to the

---

* Corresponding authors.
E-mail addresses: zhige@sdu.edu.cn (Z. Ge), hzzhang@sdu.edu.cn (H. Zhang).

https://doi.org/10.1016/j.matdes.2024.112841
Received 27 November 2023; Received in revised form 3 March 2024; Accepted 9 March 2024

Table 1
Oxide compositions of the P·I 42.5 cement (%) [44].

Materials	SiO_2	Al_2O_3	Fe_2O_3	CaO	MgO	SO_3	Na_2O	LOI
OPC	20.08	5.09	3.81	63.41	2.06	2.33	0.55	1.72

Table 2
Mixing proportion of prepared foamed concrete [44].

Mix	Targeted wet density (kg/m^3)	w/c	Cement (kg/m^3)	Water (kg/m^3)	Foam (kg/m^3)
WD600	600	0.5	386	193	20.5
WD700	700	0.5	454	227	18.8
WD800	800	0.5	521	261	17.2

Table 3
Loading speeds of specimen for compression test.

Series	Dimension (mm)	Loading speed (mm/min)
I	10 × 10 × 10	0.1
	20 × 20 × 20	0.2
	40 × 40 × 40	0.4
	70.7 × 70.7 × 70.7	0.7
	100 × 100 × 100	1
II	10 × 10 × 20	0.2
	20 × 20 × 40	0.4
	40 × 40 × 80	0.8
	70.7 × 70.7 × 141.4	1.4
	100 × 100 × 200	2

possibility of merging and overlapping of air-voids at high porosity. In general, compression tests are performed on small specimens according to relevant standards and code requirements. Considering the well-known size effect (i.e., smaller-sized specimens have higher strength than larger-sized samples), an important question is how to extrapolate the measured strengths obtained from small specimens to real full-scale structures.

Over the past few decades, several size effect laws for concrete have been proposed and implemented. They include ones based Weibull's statistical theory [17,18], Carpinteri's multifractal scaling law (MFSL) [19–21], Bažant's size effect law [22–24], and boundary effect model [25,26]. The size effect laws derived from Weibull's statistical theory was established based on the weakest link theory. As the size of the structure increases, a corresponding decrease in its nominal strength occurs because it has a higher probability of containing larger and more severe defects [18]. Carpinteri's MFSL was derived from the fractal characteristics of the microcrack structure at the maximum stress [20]. The fractal theory is utilised to characterise the damage and fracture of quasi-brittle materials in a non-integer-dimensional fractal space. Bažant's size effect law can be categorised into two groups—type-1 and type-2 size effects—depending on the adopted fracture mechanics [27–30]. The type-1 size effect manifests as specimen failure as soon as macroscopic cracks originate from the smooth surface. It can be divided into deterministic and statistical size effects based on whether the influence of randomness on material strength is considered. In the three-point bending test, the generated position of the macroscopic crack is virtually deterministic, even in the absence of preexisting notches. This deterministic size effect is primarily driven by strain concentration. In a four-point bending or direct tension test, material heterogeneity is considered by introducing the statistical size effect because the high-stress region occupies a considerable portion of the structure. The type-2 size effect occurs in quasi-brittle materials with cracks or notches that are significantly larger than the fracture process zone (FPZ) at maximum load. The boundary size effect theory was proposed by Hu and Wittmann [25,26]. This theory suggests that the size effect is not caused by the physical dimensions of the specimen but by the interaction between its FPZ and boundary conditions [31,32]. It refers to the influence of crack size on the nominal strength of the failed specimen. All the foregoing models have been applied to concrete and have shown satisfactory results. However, none of these methods have been applied to foamed concrete.

With advancements in computer facilities and algorithms, numerical simulations have emerged as a supplementary method for exploring the size effect of cementitious materials [33,34]. Different numerical approaches, such as the cohesive model [35], crack band model [36], nonlocal continuum damage model [37,38] and discrete element method [39], have been used to simulate the size effect of cementitious materials. The discrete lattice model, which considers the material structure, offers valuable insights into the correlation between fracture processes and material structures. In the present investigation, a two-dimensional lattice fracture model was established using a multiscale numerical approach [40] to study the size effect on foamed concrete. Specimens with a wet density of 700 kg/m^3 were produced and evaluated to verify the proposed modelling approach. The porous material structure used in the numerical simulation was derived by X-ray

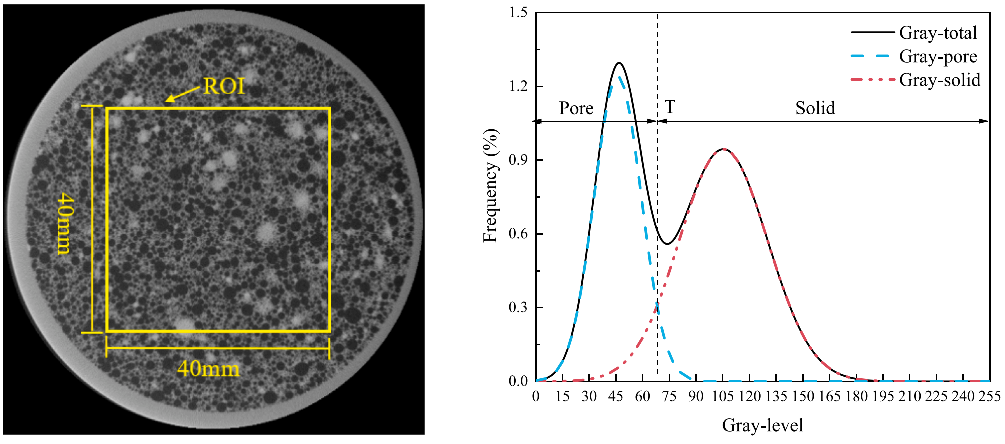

(a) (b)

Fig. 1. (a) Schematic of ROI extraction from X-CT image; (b) Phases evolution through greyscale level histogram of CT images [44].

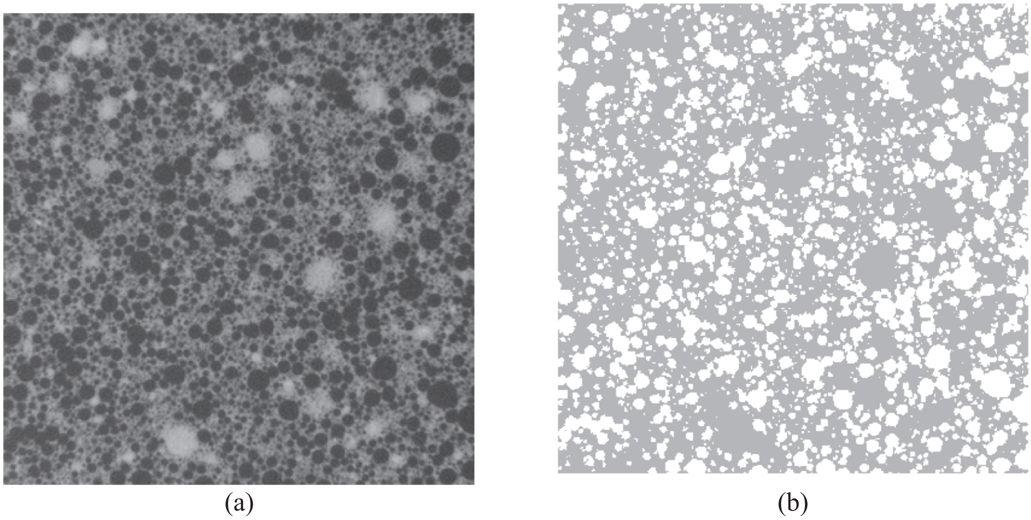

Fig. 2. Comparison of the image before and after image segmentation. (a) original grayscale image;(b) air void (white) and solid phases (grey) are isolated from the grey-scale map [44].

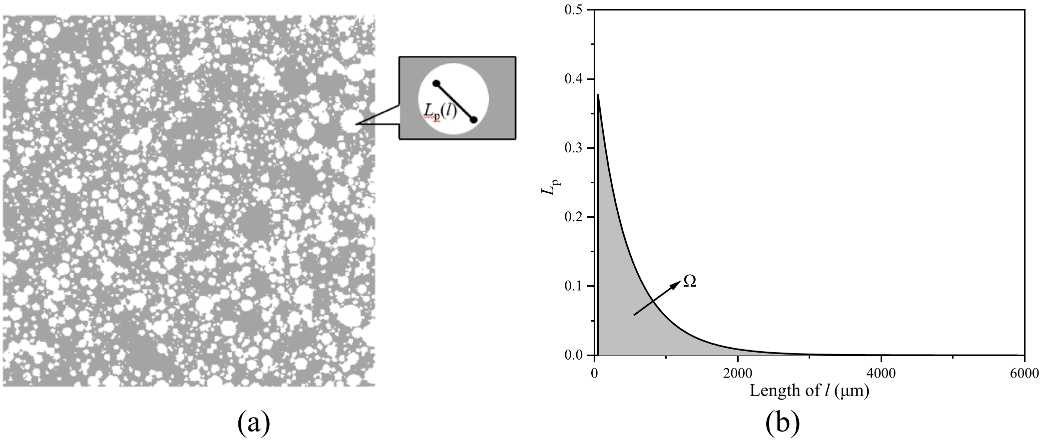

Fig. 3. (a) An entire line l with an arbitrary orientation and length in the pore phase. (Grey region: solid HCP; White region: air-void), (b) An example of L_p. Ω is the integration of the lineal-path function.

computed tomography (X-CT) and image segmentation technique. A lineal-path function [41–43] was used to describe the air void structural characteristics. Based on the observed data from the lattice model, random forest regressor (RFR) was used to predict the compressive strength of foamed concrete considering the wet density, L_p area (Ω), and specimen size as inputs. Overall, the applicability of existing analytical size effect theories to foamed concrete is tested and examined.

2. Experiment

2.1. Materials

Standard 42.5 Portland cement (Fushun Cement Group, China) was used to produce cement paste as matrix. The oxide compositions are listed in Table 1. A protein-based foaming agent (Chilong Building Energy Saving Technology Co. Ltd., China) was used to generate the foams. The foaming agent were diluted by deionized water at a volume ratio of 1:49 and the expansion ratio was within 1000–1200.

2.2. Sample preparation

Table 2 summarises the mixing ratios of foamed concrete; the water-to-cement (w/c) ratio is 0.5. The designed wet densities are 600 (WD600), 700 (WD700), and 800 kg/m^3 (WD800) by adjusting the foam volume. A pre-foaming technique was employed during mixture preparation [2]. This procedure is described in detail in a previous study of the authors [44]. After mixing, the fresh foamed concrete was cast into moulds, and all specimens were covered with plastic films. After 24 h, the samples were removed from moulds and cured at (20 ± 2) °C and (95 ± 5) % relative humidity for 28 d.

Both the X-CT scanning and uniaxial compression tests were conducted on WD700. For WD600 and WD800, X-CT scanning was performed to determine the digital material structure. The specimens for X-CT scanning were cylindrical (Ø75 mm × 200 mm). To investigate the effect of slenderness ratio on compressive strength, two series of specimens were designed with height-to-width ratios of 1 and 2. The sizes of loaded square sections were 10, 20, 40, 70.7, and 100 mm.

2.3. Mechanical loading

The loading speeds used in the compression tests are listed in Table 3. To avoid the influence of strain rate on compressive strength [45,46], a consistent axial strain rate was maintained across all specimens (e.g. 10^{-2} min^{-1}). Specimens with dimensions of 10 mm × 10 mm × 10 mm and 10 mm × 10 mm × 20 mm were tested using a mini-tension/compression stage (Mtest1000-K, China) with a loading capacity of 1

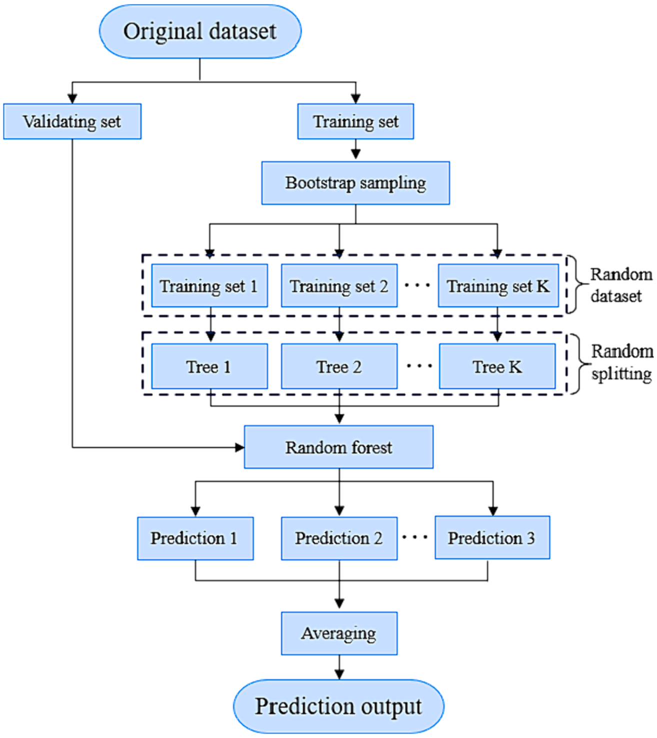

Fig. 4. Schematic of random forest generation and prediction.

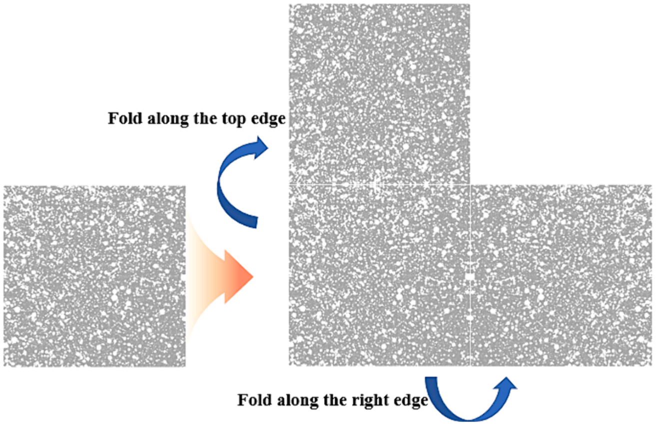

Fig. 5. Process of splicing large specimens using 40 × 40 mm X-CT images.

kN and precision of 0.001 N. Larger specimens were tested using an electrohydraulic universal testing machine (WDW-100, China) with a loading capacity of 10 kN and precision of 0.1 N. A rigid plate was used for the compression testing.

2.4. Digital specimens

A micro-XCT system (ZEISS Xradia 510 Versa) was used to obtain raw greyscale images. The working voltage and current were 140 kV and 72 mA, respectively. For each scan, the sample was rotated by 360° about the vertical axis. A total of 2000 shadow projections were obtained, each with dimensions of 1004 × 1024 pixels and a pixel size of 100 μm. The X-CT images were reconstructed using Dragonfly software. The analyses were conducted on a region of interest (40 mm × 40 mm ×

Table 4
Input parameters of the lattice model derived from [62].

Element type	Elastic modulus (GPa)		Tensile strength (MPa)	
	m	η	m	η
HCP	4.27	20.85	3.40	17.86

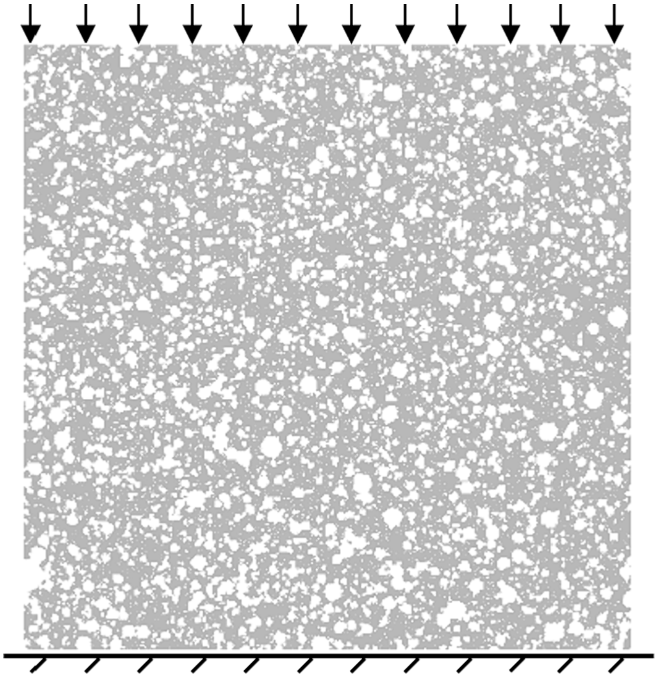

Fig. 7. Boundary condition of uniaxial compression [44].

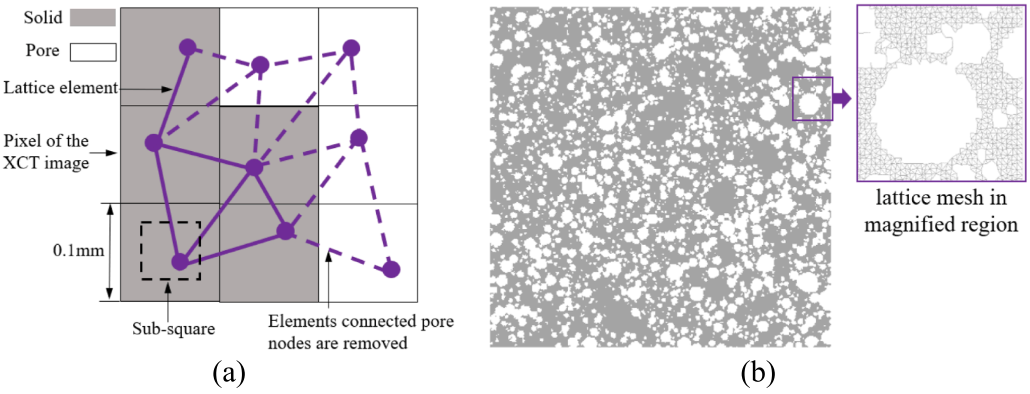

Fig. 6. (a) overlay procedure for a 2D lattice mesh; (b) 2D lattice mesh of foamed concrete after the overlay procedure using X-CT image [44].

Table 5
Summary of test results for each specimen size.

Series	Section size (mm)	Number of specimens	Average strength (MPa)	Standard deviation	CoV (MPa)
I	10 × 10 × 10	10	3.95	0.50	0.127
	20 × 20 × 20	10	3.46	0.34	0.098
	40 × 40 × 40	10	3.05	0.21	0.070
	70.7 × 70.7 × 70.7	3	2.83	0.13	0.046
	100 × 100 × 100	3	2.61	0.12	0.046
II	10 × 10 × 20	10	3.83	0.46	0.120
	20 × 20 × 40	10	3.32	0.30	0.090
	40 × 40 × 80	10	2.91	0.19	0.065
	70.7 × 70.7 × 141.4	3	2.67	0.13	0.049
	100 × 100 × 200	3	2.46	0.09	0.037

40 mm) from the core of the specimen to avoid edge hardening (Fig. 1(a)). A deconvolution approach [47,48] was adopted to determine the threshold value that decomposed the distribution curve into a sum of Gaussian functions [49]. The intersection of the two Gaussian curves was consequently defined as the threshold of the grey value (T) between the air void and solid hydrated cement paste (HCP), as shown in Fig. 1(b). This threshold is then used for image segmentation, as shown in Fig. 2. Then the porosity could be obtained by the ratio of air void in foamed concrete.

A lineal-path function and pore size distribution were used to characterise the air void structure. Calculation of pore size distribution was performed using a procedure presented by Dong et al [50]. According to their procedure, pores with a diameter larger than twice the X-CT image resolution can be calculated. The lineal-path function is characterised as a low-order descriptor derived from a more complex fundamental function capable of describing certain information regarding phase connectivity [41,43]. L_p refers to the probability of placing an entire line, *l*, with an arbitrary orientation and length in the air void phase, as shown in Fig. 3(a). A representative example of a lineal-path function is shown in Fig. 3(b). When length *l* approaches zero (the minimum length is one pixel in this study), L_p represents the void volume fraction. As the length of *l* gradually increases, L_p gets small and approaches 0. When *l* is longer than the maximum pore size, L_p is equal to 0. The Ω depicted in Fig. 3(b) is acquired through the integration of the probability, L_p, with length *l*, as given by Eq. (1). Here, Ω was used to characterise the foamed concrete microstructure.

$$\Omega = \int_0^\infty L_p(l)dl \tag{1}$$

3. Random forest regressor

The RFR model has been widely utilised in classification and regression tasks through the generation of numerous classification or regression trees incorporating bootstrap and aggregation concepts [51,52]. A schematic of random forest generation and prediction is shown in Fig. 4. Each tree in the forest is constructed using a random training set, and each split within each tree is generated based on a subset of input variables that are randomly selected [53]. All the trees in

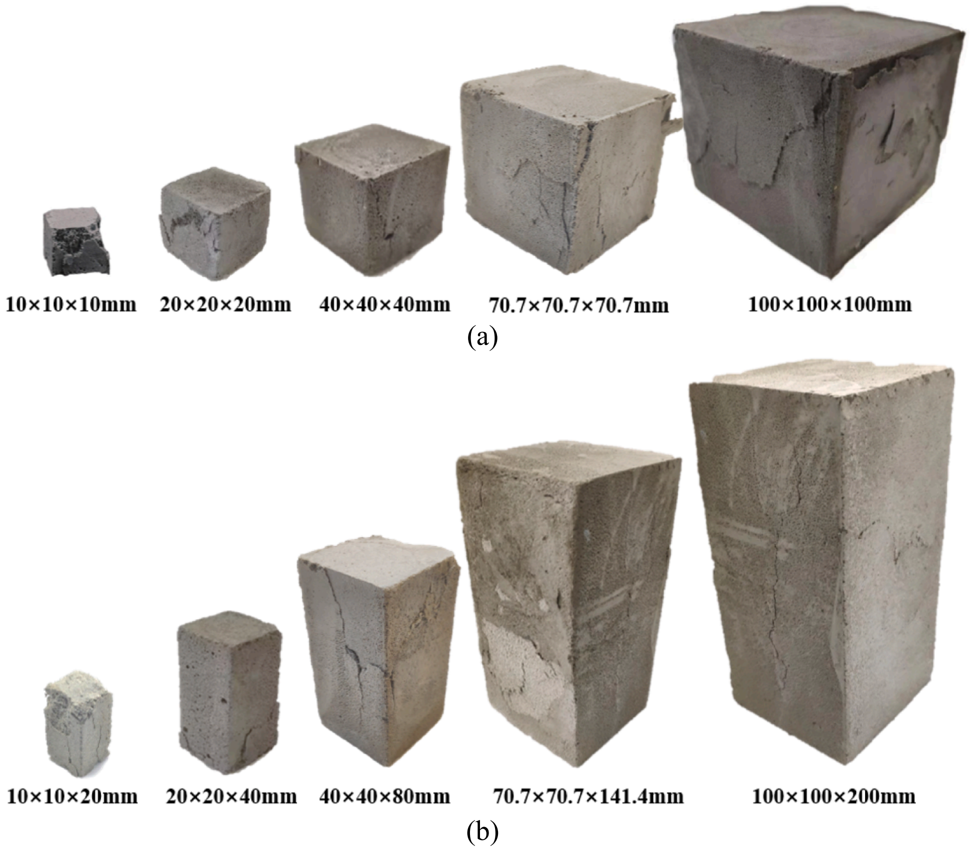

Fig. 8. Typical crack pattern of WD700 specimens at the failure stage: (a) Slenderness ratio = 1; (b) Slenderness ratio = 2.

Table 6
Summary of simulated results of each specimen size.

Mix	Model size (mm)	Number of models	Compressive strength (MPa)	Elastic modulus (GPa)
WD600	10 × 10	10	2.97 ± 0.45	1.53 ± 0.23
	20 × 20	10	2.63 ± 0.37	1.49 ± 0.26
	40 × 40	10	2.40 ± 0.22	1.48 ± 0.21
	70.7 × 70.7	3	2.21 ± 0.19	1.52 ± 0.22
	100 × 100	3	1.97 ± 0.12	1.47 ± 0.25
	10 × 20	10	2.74 ± 0.36	1.49 ± 0.23
	20 × 40	10	2.43 ± 0.24	1.46 ± 0.24
	40 × 80	10	2.18 ± 0.20	1.45 ± 0.21
	70.7 × 141.4	3	1.95 ± 0.17	1.46 ± 0.22
	100 × 200	3	1.85 ± 0.11	1.45 ± 0.23
WD700	10 × 10	10	3.93 ± 0.38	2.02 ± 0.22
	20 × 20	10	3.26 ± 0.31	1.98 ± 0.19
	40 × 40	10	2.88 ± 0.23	1.96 ± 0.16
	70.7 × 70.7	3	2.77 ± 0.15	2.08 ± 0.18
	100 × 100	3	2.57 ± 0.10	1.97 ± 0.15
	10 × 20	10	3.59 ± 0.33	2.04 ± 0.20
	20 × 40	10	3.20 ± 0.25	1.94 ± 0.16
	40 × 80	10	2.78 ± 0.18	2.06 ± 0.17
	70.7 × 141.4	3	2.59 ± 0.13	2.01 ± 0.21
	100 × 200	3	2.50 ± 0.11	1.97 ± 0.18
WD800	10 × 10	10	4.57 ± 0.31	2.72 ± 0.17
	20 × 20	10	4.17 ± 0.21	2.69 ± 0.18
	40 × 40	10	3.85 ± 0.18	2.63 ± 0.15
	70.7 × 70.7	3	3.60 ± 0.08	2.70 ± 0.12
	100 × 100	3	3.47 ± 0.09	2.67 ± 0.13
	10 × 20	10	4.35 ± 0.37	2.63 ± 0.21
	20 × 40	10	3.84 ± 0.22	2.78 ± 0.19
	40 × 80	10	3.54 ± 0.15	2.71 ± 0.14
	70.7 × 141.4	3	3.36 ± 0.12	2.66 ± 0.12
	100 × 200	3	3.27 ± 0.11	2.61 ± 0.13

the forest were mature binary trees.

The random forest algorithm encompasses various hyperparameters that influence its structure and performance [54,55]. In the current study, the hyperparameters of the algorithm are as follows. The number of generated regression trees (*K*) is fixed at 100, and the minimum numbers of samples within each leaf node and non-leaf node are 1 and 2, respectively.

The RFR model was assessed using correlation coefficient (*r*), root mean square error (*RMSE*), mean absolute error (*MAE*), and mean absolute percentage error (*MAPE*). The mathematical expressions are given by Eqs. (2)–(5). The precision of the model is assessed based on the error accumulation of *MAE* and *RMSE*. The relative error between the predicted and measured values is indicated by *MAPE*. Therefore, the lower the values of *MAE*, *MAPE*, and *RMSE*, the higher the accuracy in predicting the compressive strength of foamed concrete. The equations used in the assessment are as follows:

$$r = \frac{\sum_{i=1}^{n}(s_i - \overline{s}_i)(m_i - \overline{m}_i)}{\sqrt{\sum_{i=1}^{n}(s_i - \overline{s}_i)^2(m_i - \overline{m}_i)^2}} \tag{2}$$

$$RMSE = \sqrt{\frac{\sum_{i=1}^{n}(s_i - m_i)^2}{n}} \tag{3}$$

$$MAPE = \frac{1}{n}\sum_{i=1}^{n}\left|\frac{s_i - m_i}{s_i}\right| \times 100 \tag{4}$$

$$MAE = \frac{\sum_{i=1}^{n}|s_i - m_i|}{n} \tag{5}$$

where *n* is the size of the dataset; s_i is the individual strength measured using the lattice model; m_i is the predicted strength; and $\overline{s_i}$ and $\overline{m_i}$ are the mean strength values.

4. Modelling

Lattice fracture models are typically employed to simulate the deformation and fracture behaviour of quasi-brittle materials [56,57]. These models have been demonstrated useful for studying the size effect on mechanical properties because of its inherent simplicity [58,59]. They include the assumption of linear elastic fracture behaviour of a local lattice element and the straightforward implementation of material heterogeneity at different length scales. This allows the investigation of fracture mechanisms and size effects on the mechanical properties in a manner consistent with laboratory tests [59].

In the discrete lattice model, the material is discretised as a system of Timoshenko beams that consider shear deformation [40]. Each element represents a small volume of the material. The generation of the beam network is as follows. The domain is first partitioned into a number of square cells matching each pixel. Subsequently, a node is randomly placed inside each cell. The ratio between the size of the cell and pixel is characterised by mesh randomness, which serves as an indicator of the disorder level in the lattice mesh. Randomness not only influences the simulated fracture pattern [60] but also governs the Poisson's ratio of the mesh. A mesh randomness value of 0.5 leads to a Poisson's ratio of

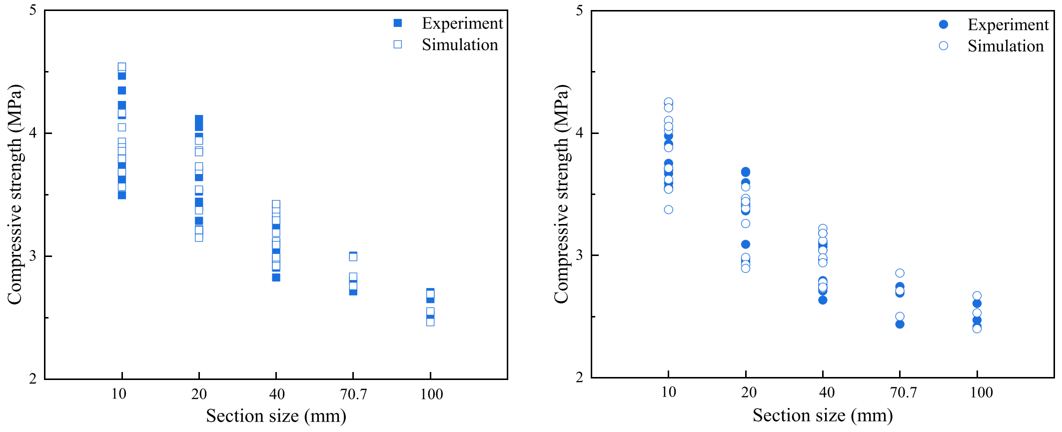

(a) (b)

Fig. 9. Compressive strength of experiment and simulation for WD700: (a) Slenderness ratio = 1; (b) Slenderness ratio = 2.

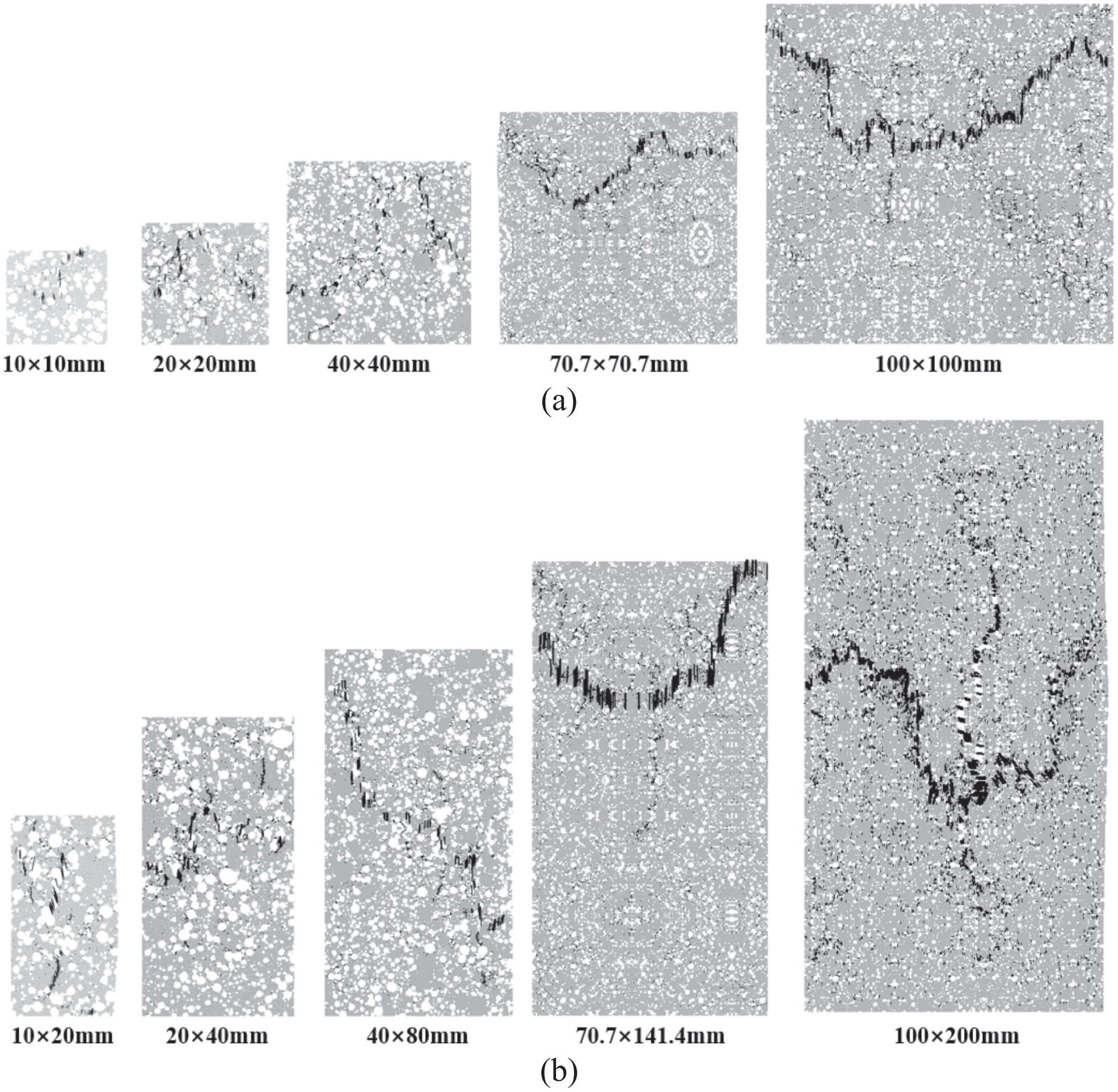

Fig. 10. Typical crack pattern of WD600 specimens at the failure stage: (a) Slenderness ratio = 1; (b) Slenderness ratio = 2.

0.18 for a global system. This is consistent with cementitious materials. Therefore, a randomness value 0.5 is adopted. Subsequently, the nodes are connected to each other through Delaunay triangulation [61] to form a lattice network.

Due to the limitation of the specimen size scanned by the X-CT, digital specimens with dimensions of 70.7 × 70.7 mm, 70.7 × 141.4 mm, 100 × 100 mm and 100 × 200 mm were spliced by the X-CT images with size of 40 × 40 mm. The splicing process is shown in Fig. 5. The digital specimen with size of 40 × 40 mm is folded along the top and the right edge to acquire the target sized specimen.

Elements with one end in air voids are removed from the lattice network, as shown in Fig. 6(a). The final lattice network of foamed concrete is shown in Fig. 6(b). The input mechanical parameters for the elements were obtained from the outcomes of micromechanical modelling previously conducted by the authors [62]. The adopted mesoscale resolution corresponded to the dimensions of the material volume investigated in [62]. Further elaboration on micromechanical modelling is found in [63,64]; insights into multiscale modelling strategies are provided by [65]. The input parameters for the solid HCP elements are assumed to follow the Weibull distribution (Eq. (6)):

$$F(x) = 1 - \exp\left[-\left(\frac{x}{\eta}\right)^{m}\right] \tag{6}$$

where x represents the tensile strength or elastic modulus; η is the scaling parameter; and m is the shape parameter. The parameters used are listed in Table 4.

A computational uniaxial compression test is conducted by imposing a nodal displacement at one end and fixing the other end, as shown in Fig. 7. Considering the horizontal constraint resulting from the friction between the specimen and steel plates, the lateral deformation and rotation are restricted at both ends. A sequence of linear elastic analyses is performed by computing the stress on each beam element. Normal force and bending moment are considered in the stress calculations:

$$\sigma = \alpha_N \frac{N}{A} + \alpha_M \frac{M}{W} \tag{7}$$

where N is the normal force along the element; M is the bending moment in the local coordinate system; A is the cross-sectional area of the beam; and W is the cross-sectional moment of resistance. Parameters α_N and α_M represent the influence factors of normal force and bending moment, respectively; the commonly adopted factor values are 1.0 and 0.5, respectively [57]. The influence of these parameters on the fracture behaviour is discussed in [66].

An experimental compression test was conducted on a series of samples with various WD700 sizes to verify the proposed modelling

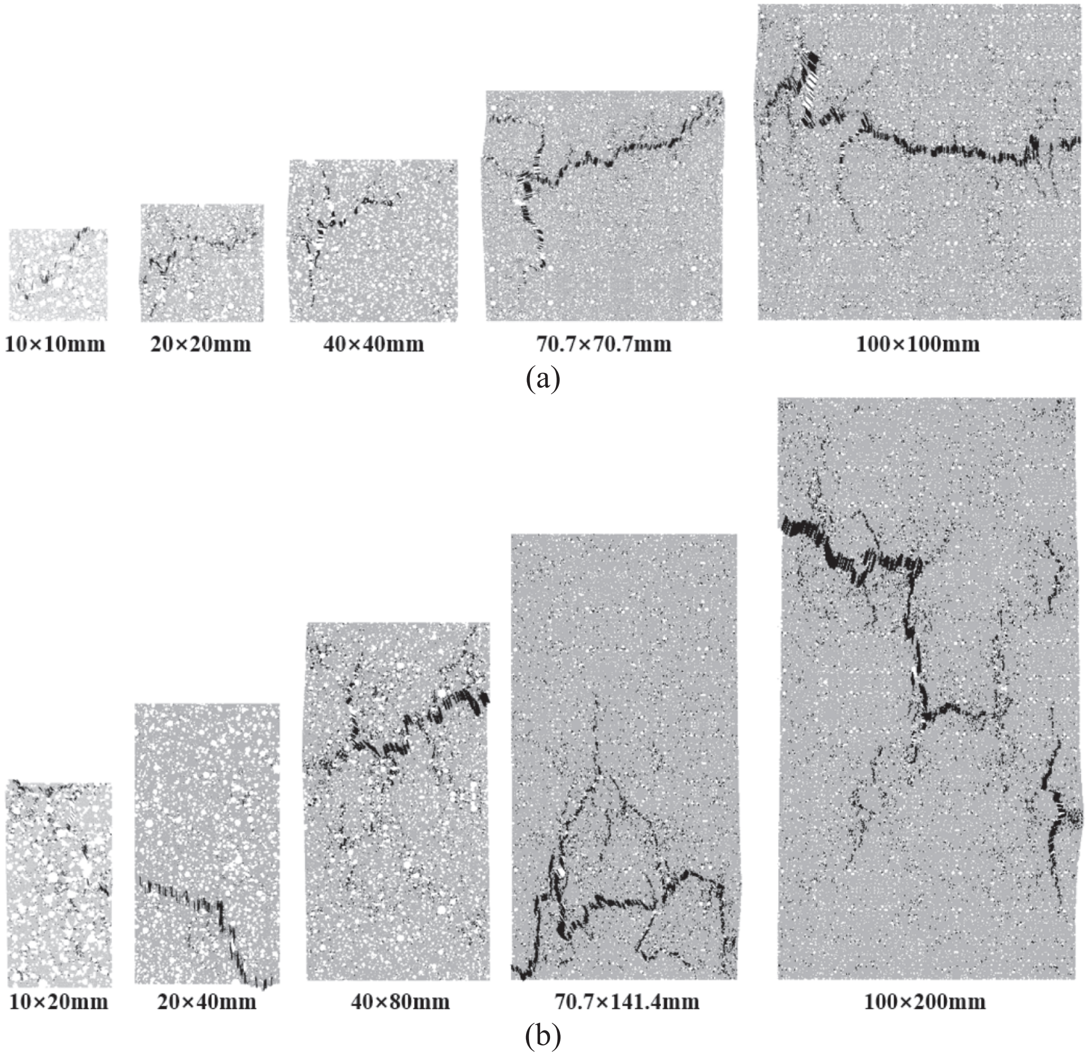

Fig. 11. Typical crack pattern of WD700 specimens at the failure stage: (a) Slenderness ratio = 1; (b) Slenderness ratio = 2.

strategy. The fracture model was used to investigate the size effect of foamed concrete with different densities. It should be noted that the air void structure derived from X-CT scanning varies for mixes with different densities but input parameters for the solid elements are the same as the water/binder ratio is kept as 0.5 for all mixes.

5. Results and discussions

5.1. Experiments

Table 5 lists the measured average strengths, standard deviations, and coefficient of variation (CoV) of WD700. The compressive strength ranges 2.62–3.95 MPa for specimens with a slenderness ratio of 1. The strength increased by 51 % when the volume decreased by 1000 times. When the slenderness ratio was 2, the measured compressive strength decreased. This phenomenon was also observed in HCP [67] and concrete [68]. It was attributed to the effect of the end restraint due to the friction between the rigid steel plates and specimen. A wide scatter in the measured strength was observed among specimens with relatively small dimensions. As the specimen size increases, the standard deviation and CoV decrease. Owing to the significant influence of the spatial distribution of air voids on the failure of relatively small specimens, a wide scatter in measured strengths occurs [69,70].

The fracture patterns observed in specimens of different sizes at the failure stage are shown in Fig. 8. The cracks in the cubic specimens, mainly in the diagonal direction, follow a tortuous path, as shown in Fig. 8(a). Two types of cracks are observed in the prismatic specimens. The first follows the diagonal direction, whereas the second is virtually parallel to the direction of loading (Fig. 8(b)); the reason for this is discussed in Section 4.2.2. No cracks were observed at the two ends of the cubic and prismatic specimens owing to the confinement provided by the rigid steel plates. The fracture patterns (several inclined main cracks along the loading direction) of the specimens of different sizes were not the same owing to the stochastic spatial distribution of air voids.

5.2. Modelling

5.2.1. Compressive strength

The simulated compressive strengths are listed in Table 6. Evidently, as the density of the foamed concrete increases, the concrete's ultimate load-bearing capacity increases. This is primarily because the specimens with a high wet density have low porosity. The effects of the geometric dimensions and slenderness ratio on the compressive strength were simulated using the model. As the specimen size increases, the compressive strength and variability decrease. A low compressive strength was observed in the specimens with high slenderness ratios (prismatic specimens). Furthermore, as shown by the values summarised in Table 6, the simulated elastic modulus is relatively insensitive to variations in specimen geometry. This insensitivity is mainly influenced

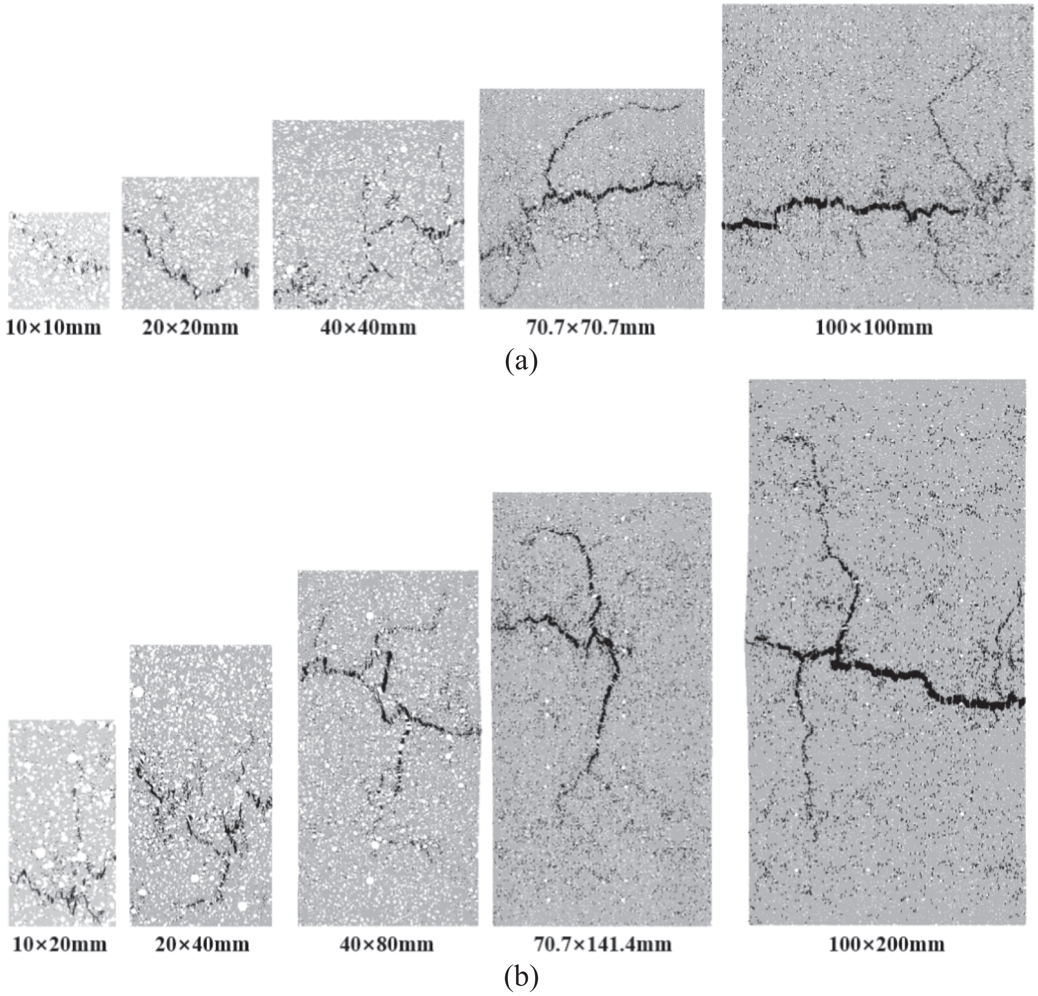

Fig. 12. Typical crack pattern of WD700 specimens at the failure stage: (a) Slenderness ratio = 1; (b) Slenderness ratio = 2.

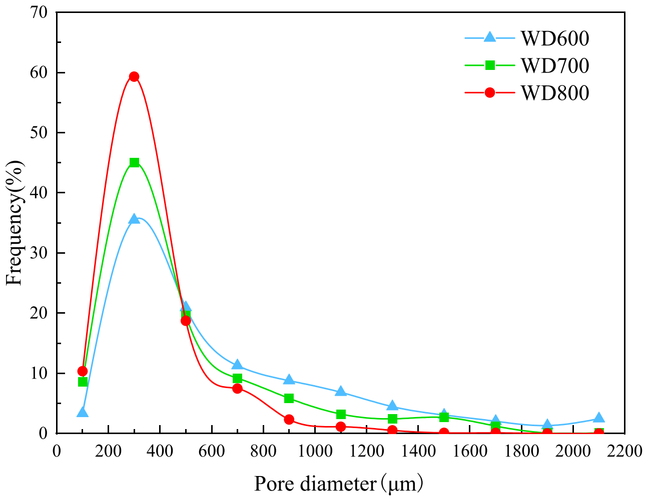

Fig. 13. Pore diameter distribution.

by the properties and proportions of material components and not by the boundary conditions, as is the case for the compressive strength.

A comparison between the simulated and measured compressive strengths of WD700 is shown in Fig. 9. The compressive strength predicted by the lattice model was in excellent agreement with the experimental results. This shows that the proposed lattice model can simulate the strength and crack patterns of foam concrete of different sizes.

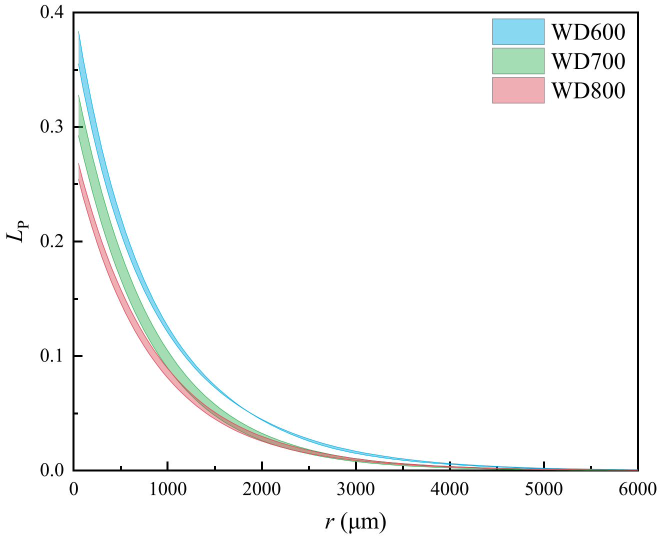

Fig. 14. lineal-path functions (L_p) for three mixtures.

Table 7
L_p area of foamed concrete for each mix.

Mix	Porosity (%)	L_p area (Ω)
WD600	37.72 ± 1.39	329.36 ± 7.27
WD700	30.59 ± 1.24	261.06 ± 5.50
WD800	24.38 ± 1.23	226.28 ± 1.84

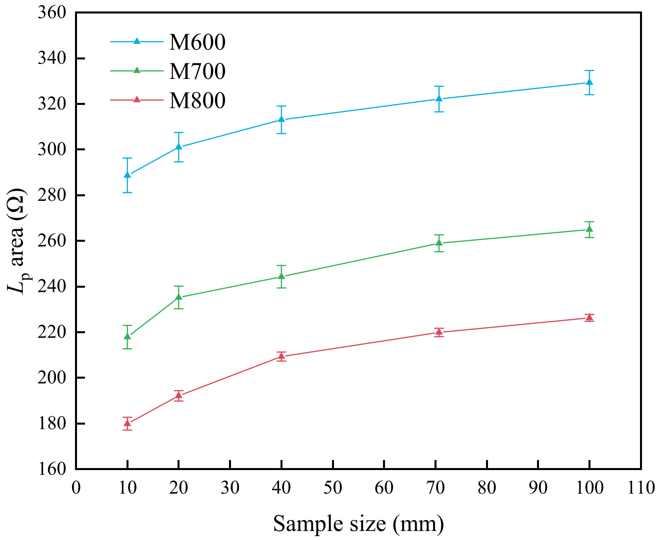

Fig. 15. Variation of Ω with specimen size.

5.2.2. Crack patterns

Typical simulated crack patterns at the failure stage are shown in Fig. 10, Fig. 11 and Fig. 12 for WD600, WD700, and WD800, respectively. The main cracks are inclined along tortuous and diagonal paths in the square specimens. In the rectangular specimens, the cracks are oriented along the diagonal direction and parallel to the loading orientation; this is consistent with the experimental results. Because the boundary conditions for loading remain the same, the difference in the main crack can be attributed to the variation in the air void structure. In contrast to cement paste [67] and concrete [71] in which main cracks are usually identified, the crack pattern in foamed concrete exhibits widespread microcracks in addition to several main cracks. This observation is due to the complex internal air void structure of foamed concrete. Pore configuration and distribution significantly influence crack propagation and contribute to the final crack pattern [72,73].

5.3. Pore structure

The 3D pore size distribution is shown in Fig. 13. The percentages of the pores with diameter between 100 μm and 500 μm of WD600, WD700 and WD800 are 59.76 %, 73.22 % and 88.39 %, respectively. In addition, it is found that the pore size distribution range of WD600 is wider compared to the other two. For a given size of foamed concrete specimen, a decrease in density means the decrease of HCP volume and the increase of foam volume. And there is a positive correlation between the air-void merger rate and the foam volume [74]. Therefore, the higher density, the smaller the probability of air-void merging, and the pore size distribution develops towards a narrower direction.

The lineal-path functions derived from 10 segmented X-CT images with dimensions of 1000 × 1000 pixels (100 mm × 100 mm) are shown in Fig. 14. The shaded area represents the upper and lower bounds of the

Table 8
Fitting results of air-void structure parameter and strength.

Parameter	r	Fitting curve	R^2
Porosity-Strength	−0.8502	Y = -0.1476X + 7.856	0.7229
L_p area (Ω)-Strength	−0.9143	Y = -0.0153X + 7.098	0.8360

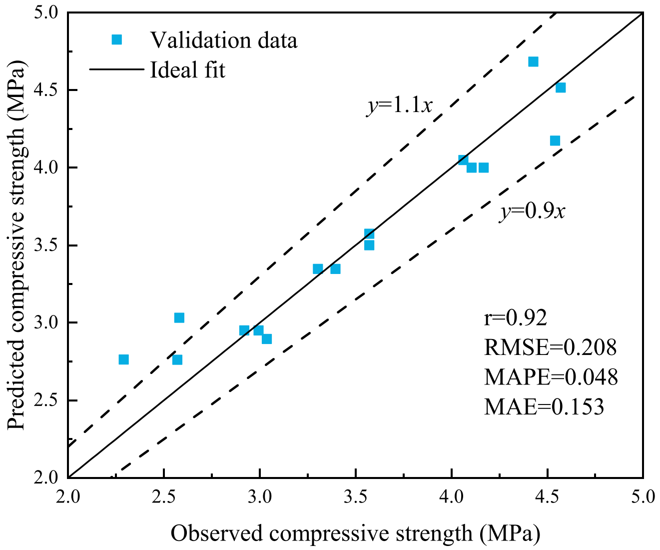

Fig. 17. Comparison of observed and predicted results.

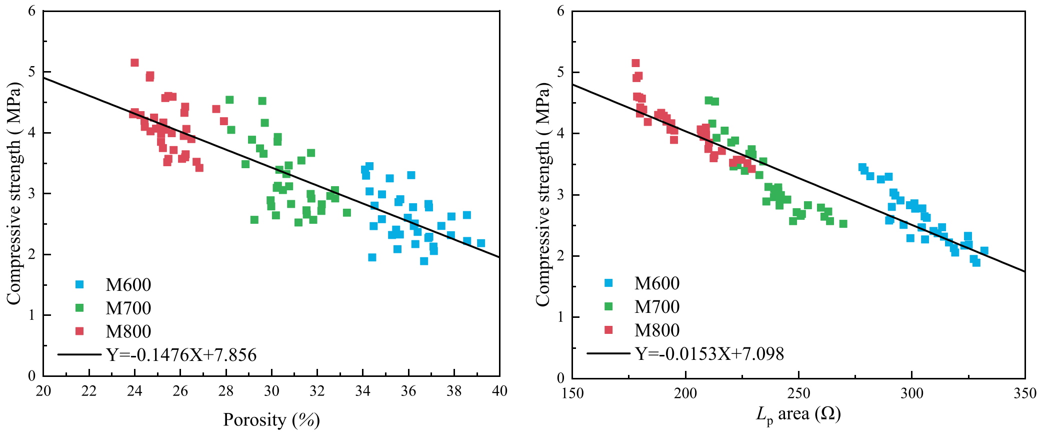

(a) (b)

Fig. 16. Correlation between air-void structure parameter vs compressive strength: (a) Porosity-Strength, (d) L_p area (Ω)-Strength.

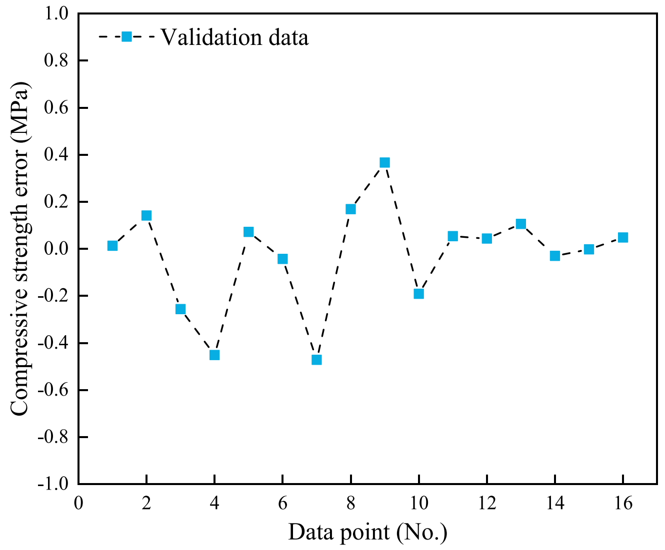

Fig. 18. Error analysis.

lineal-path functions from the 10 images. The average Ω is calculated and listed in Table 7. An inverse relationship between Ω and wet density is observed. This indicates that the specimens with higher wet density have smaller void clusters. This is consistent with the pore size distribution analysis in which foamed concrete with higher density has a narrower pore size distribution and more pores concentrates in a small size range.

The calculated Ω for different sample sizes is shown in Fig. 15. Evidently, Ω increases and stabilises as the specimen size increases. Furthermore, smaller specimens with the same wet density have the lower Ω. This is primarily because small specimens have a lower probability of containing larger air voids, resulting in smaller void clusters. When the specimen size decreases from 100 to 10 mm, the Ω values reduce by 12.3 % for WD600, 17.8 % for WD700, and 20.4 % for WD800. This indicates that the heterogeneity of the air void structure becomes more evident as the specimen size decreases.

The fitted porosity–strength and Ω–strength relationships are shown in Fig. 16. The fitting results are summarised in Table 8. The compressive strength exhibits a linear relationship with both porosity and Ω. The correlation coefficient, r, between porosity and strength is − 0.8502, whereas the r value between Ω and strength is − 0.9143. This indicates that the correlation of Ω with compressive strength exceeds that with porosity.

Table 9
Parameters of fitting Weibull size effect equation.

Mix	Slenderness ratio	a	m	R^2
WD600	1	0.630	11.85	0.9674
	2	0.610	11.53	0.9753
WD700	1	0.770	13.95	0.9840
	2	0.742	14.04	0.9989
WD800	1	0.877	16.76	0.9989
	2	0.852	16.42	0.9749

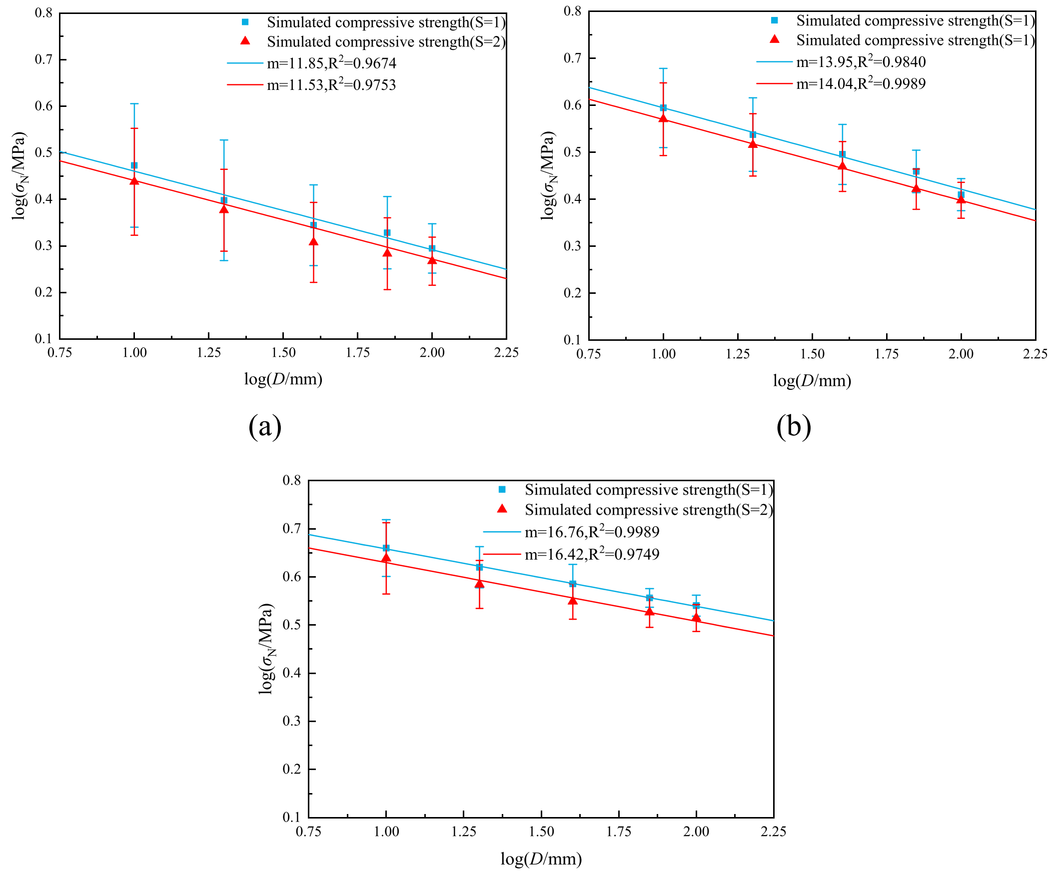

(a)

(b)

(c)

Fig. 19. Fits of Weibull weakest link theory: (a) WD600, (b) WD700, (c) WD800.

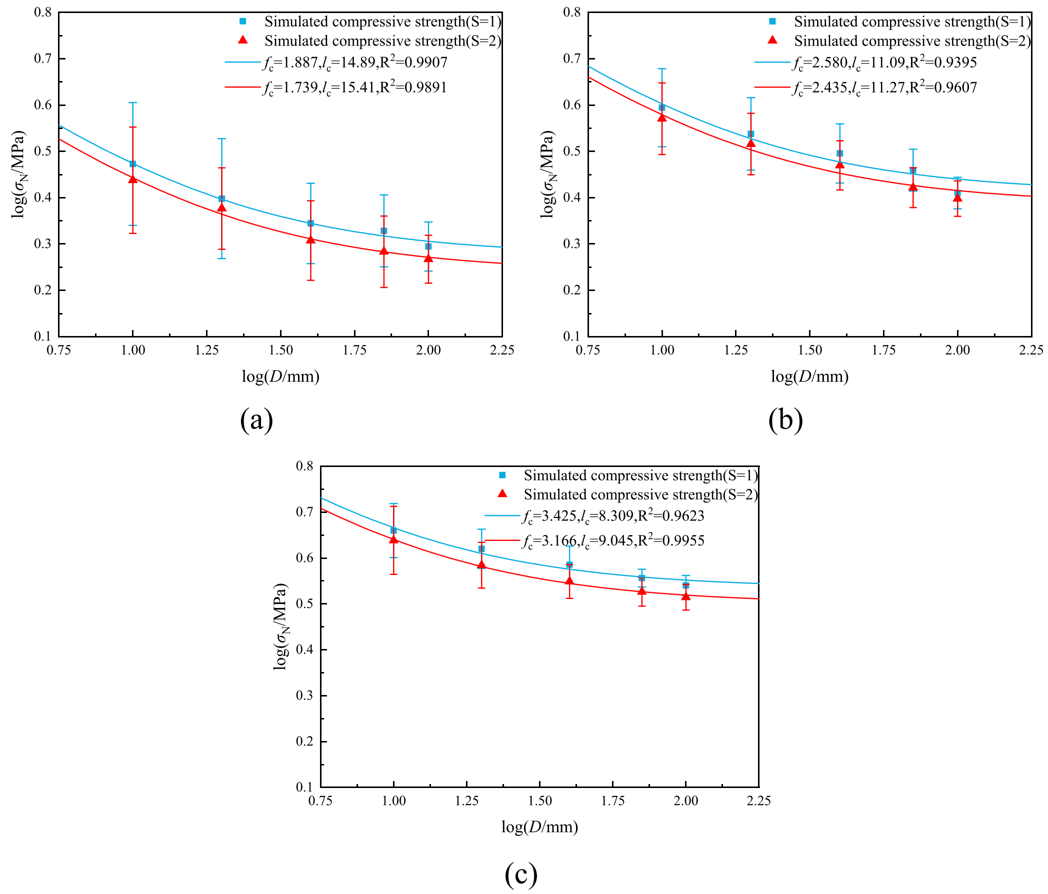

(a)

(b)

(c)

Fig. 20. Fits of Carpinteri's MFSL: (a) WD600, (b) WD700, (c) WD800.

Table 10
Parameters of fitting Carpinteri's MFSL equation.

Mix	Slenderness ratio	f_c (MPa)	l_c (mm)	R^2
WD600	1	1.887	14.89	0.9907
	2	1.739	15.41	0.9891
WD700	1	2.580	11.09	0.9395
	2	2.435	11.27	0.9607
WD800	1	3.425	8.31	0.9623
	2	3.166	9.05	0.9955

5.4. *Random forest regressor*

The model was trained using 108 simulation results from the lattice model, considering the wet density, *Ω,* and specimen size as inputs to predict the compressive strength of foamed concrete. Furthermore, 80 % and 20 % of the observations were used to train and validate the model, respectively. A regression plot of the predicted versus observed values is shown in Fig. 17. The closer the alignment of data points with the regression line ($y = x$), the stronger the predictive performance of the machine learning model [75]. Evidently, the majority of predictions are within a ± 10 % error range from the observed results ($y = x$). This suggests the absence of significant underfitting or overfitting in the RFR model. An r value of 0.92 indicates a strong correlation between the observations and predictions. The *RMSE, MAPE,* and *MAE* values are 0.208, 15.3 %, and 0.048, respectively. Results indicate a strong concordance between the observed data and predicted outcomes. This indicates that the RFR model demonstrates high accuracy in predicting the compressive strength of foamed concrete. In addition, the error analysis shown in Fig. 18 shows that the errors of compressive strength range 0–0.45 MPa.

5.5. *Fitting of analytical size effect models*

5.5.1. *Weibull size effect*

The most renowned theory regarding the statistical size effect resulting from the randomness of material strength is the Weibull statistical theory [18]. This theory was developed based on the weakest link model hypothesis, which assumed that the nominal strength of concrete was governed by the weakest elements of the structure. Based on statistics, the relationship between the nominal strength, σ_N, and structural size, D, is given by the following:

$$\log\sigma_N = a - \frac{n}{m}\log D \tag{8}$$

where σ_N is the nominal strength; D is the specimen size (i.e., section size); m is the Weibull modulus from the fitting of simulated results; and n denotes the number of dimensions.

The trust region method was employed to conduct a linear regression of simulation results (Fig. 19) [76]. The fits for the three densities showed coefficients of determination exceeding 0.96. The fitting parameters are listed in Table 9. As wet density decreases, m decreases. This indicates that foamed concrete with a high porosity is brittle. Furthermore, owing to the absence of stiff aggregates that enhance the stability of crack propagation, the values of m are lower than those of concrete reported by Vu ranging 14–34 [77]. Compared with HCP, the presence of air voids in foamed concrete renders the crack path more tortuous and enhances ductility. Thus, its Weibull modulus is higher than that of HCP [34]. The analysis also indicated that the slenderness

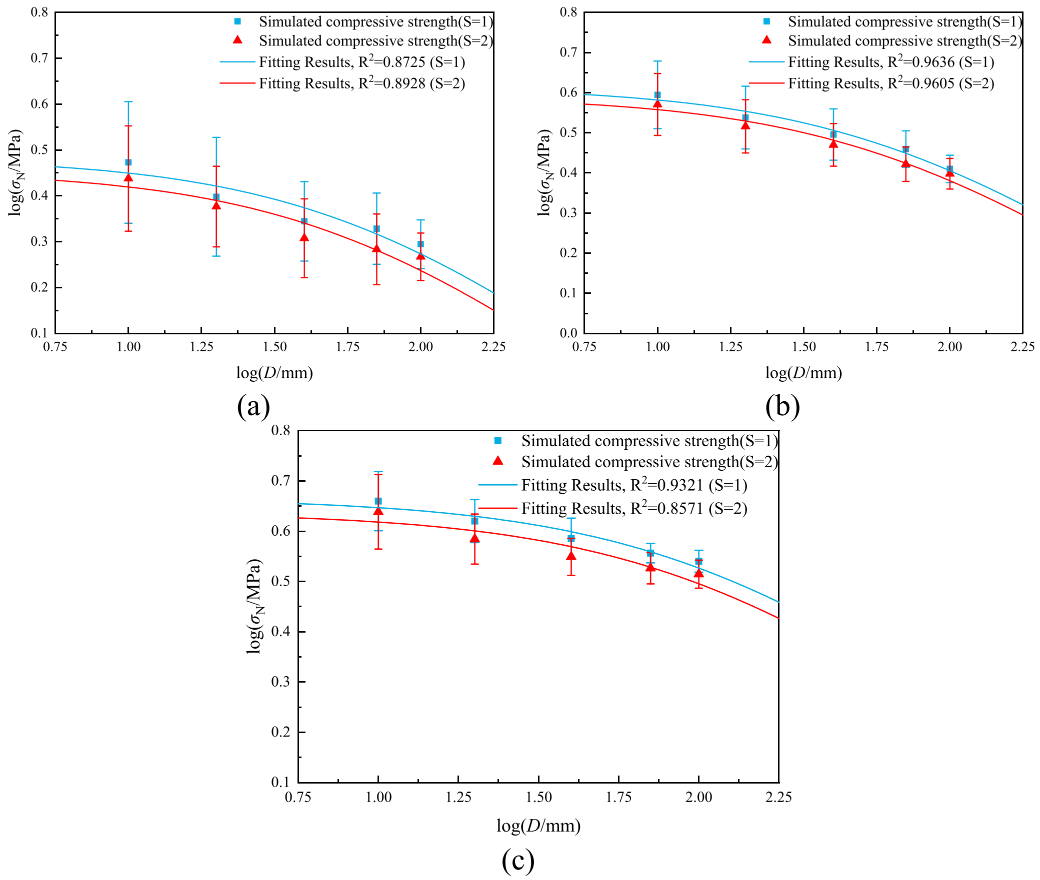

(a) (b) (c)

Fig. 21. Fits of Bažant's size effect law: (a) WD600, (b) WD700, (c) WD800.

Table 11

Parameters of fitting Bažant's size effect law.

Mix	Slenderness ratio	B	f_c	D_0	R^2
WD600	1	1.54	1.97	61.86	0.8725
	2	1.54	1.85	58.37	0.8928
WD700	1	1.60	2.57	82.90	0.9636
	2	1.56	2.50	82.30	0.9605
WD800	1	1.53	3.47	111.8	0.9321
	2	1.52	3.27	108.4	0.8571

ratio of the specimens had no significant effect on the Weibull modulus. This indicates that the Weibull modulus is mainly affected by the material structure rather than by the boundary conditions [77].

5.5.2. *Carpinteri's multifractal scaling law*

Carpinteri [78] proposed that the variation in the crack fractal properties at different observation scales was the underlying cause of the size effect in quasi-brittle materials. The equation proposed by Carpinteri for size effect is as follows:

$$\sigma_N = f_c\sqrt{1+\frac{l_c}{D}} \tag{9}$$

where σ_N is the nominal compressive strength associated with the specimen size; f_c is the theoretical strength with an infinitely large size; and l_c is the material characteristic size reflecting the influence of disorder on the mechanical behaviour. As shown in the double logarithmic graphs (Fig. 20), Eq. (9) is fitted using the trust region method. The parameters of the MFSL equation for different mixtures are obtained and listed in Table 10. The high coefficient of determination (R^2) suggests that this size effect law formula is in excellent agreement with the experimental measurements. The theoretical strength of an infinitely large specimen increases with the wet density. This is mainly because the specimens with a high wet density have a high ultimate load-bearing capacity. The characteristic particle size decreased as the wet density increased. This tendency arises because a mixture with low wet density has a large L_p area and numerous void clusters. Thus, the influence of air void structure on the variability of the compressive strength of foamed concrete decreased, and the characteristic size exhibited a downward trend with increasing wet density. The characteristic size of foamed concrete is larger than that of cement paste (l_c is ~ 8 mm) [34] and smaller than that of concrete ($l_c = 150$ mm) [45] owing to the size of the introduced air voids.

5.5.3. *Bažant's size effect law*

The type-2 size effect law proposed by Bažant [22,23] is suitable for geometrically similar specimens where a large crack (similar for different sizes) develops steadily before the maximum load is attained. The corresponding theoretical formula can be written as:

$$\sigma_N = \frac{Bf_c}{\sqrt{1+D/D_0}} \tag{10}$$

where σ_N represents the nominal strength of geometrically similar specimens; f_c represents the mean compressive strength of standard foamed concrete samples (in this study, the side length is 100 mm); D is the characteristic size of the specimen; B and D_0 are the empirical parameters determined by the optimum fitting of nominal strengths, σ_N, covering a sufficiently broad size range; and D_0 is a physical quantity related to the brittleness of the material. The fitting curves using Eq. (10)

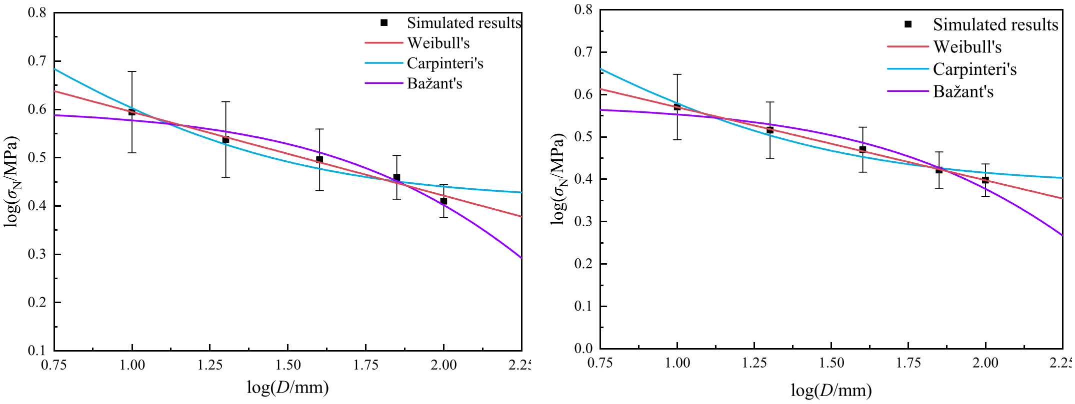

(a) (b)

Fig. 22. Comparison of the fitting result of three analytical models: (a) Slenderness ratio = 1; (b) Slenderness ratio = 2.

are shown in Fig. 21. The parameters are listed in Table 11. Evidently, the empirical parameter, B, remains relatively consistent, fluctuating within the range 1.52–1.60 among the various mixtures. This means that wet density and slenderness ratio have no significant impact on parameter B. In contrast, wet density has a significant effect on D_0. As the wet density increases, parameter D_0 exhibits an upward trend, indicating that foamed concrete with a high foam volume is more brittle, and the size effect is more evident.

5.5.4. General discussion

As shown in Fig. 22, the three analytical models can describe the change in strength with specimen size. However, this applicability requires further validation. When the specimen size is reduced to zero, the compressive strengths predicted by the three equations differ. The accuracy of the predictions of small-sized specimens is extremely difficult to validate. When the specimen is of a diminutive size, the result from fracture model loses its representativeness. This is because the material may only consist of a single HCP phase and is not a representative volume element of the material. In addition, when the specimen size increases towards infinity, the curves from the three theoretical models differ. Therefore, the conduct of large-scale fracture models for validation are necessary. However, such simulations are challenging. The challenges associated with conducting such large-scale models include modelling and the requirement of computational capability of computing equipment.

6. Conclusions

The size effect on the compressive strength of foamed concrete (size range: 10–100 mm) was investigated in this study. A discrete lattice model combining microstructures was applied to simulate the fracture responses of specimens with different sizes at the mesoscale. The area of the L_p function was used to describe the air void structure features. Based on the observed results from the lattice model, the RFR was employed to predict the strength of foamed concrete considering wet density, L_p area, and specimen size as input parameters. Existing analytical size effect theories have been employed to analyse the fracture performance of foamed concrete based on numerical results. The influence of wet density and slenderness ratio on the size effect of foamed concrete is discussed. The conclusions are summarised as follows.

- The experimental and simulation results confirm that the average compressive strength of foamed concrete and its variation decrease with increasing specimen size. The specimen size has no significant effect on the elastic modulus. The main cracks are inclined and follow a tortuous and diagonal path in both the cubic and prismatic specimens.
- The proposed *meso*-scale fracture model can predict the compressive strength of foamed concrete specimens of different sizes.
- The L_p area describes the air void structure in detail and has a stronger correlation with the compressive strength compared with porosity. In addition, the L_p area values increase and tend to stabilise as the specimen size increases. Specimens with a high wet density have small L_p areas and few void clusters.
- Using L_p area, specimen size and wet density as input, the compressive strength of foamed concrete can be predicted by RFR with high accuracy.
- The analytical models all exhibit high coefficients of determination. However, closely examining the underlying physical significance of these empirical parameters is crucial. The derived Weibull modulus of foamed concrete is between those of HCP and normal concrete. This indicates that foamed concrete is more brittle than normal concrete and less brittle than cement paste.

CRediT authorship contribution statement

Nengdong Jiang: Writing – original draft, Investigation, Data curation. **Zhi Ge:** Supervision, Methodology, Funding acquisition, Data curation. **Zhiyuan Wang:** Investigation, Data curation. **Tianming Gao:** Methodology, Investigation, Formal analysis. **Hongzhi Zhang:** Writing – original draft, Supervision, Methodology, Funding acquisition. **Yifeng Ling:** Supervision, Investigation. **Branko Šavija:** Supervision, Methodology.

Declaration of competing interest

The authors declare that they have no known competing financial interests or personal relationships that could have appeared to influence the work reported in this paper.

Data availability

Data will be made available on request.

Acknowledgments

This work was supported by Supported by National Natural Science Foundation of China(52378250), 111 Project(No.B21012), Taishan Scholar Foundation of Shandong Province (No.tsqn201909032).

References

[1] K. Ramamurthy, E.K. Nambiar, G.I.S. Ranjani, A classification of studies on properties of foam concrete, Cem. Concr. Compos. 31 (6) (2009) 388–396.

[2] A. Raj, D. Sathyan, K.M. Mini, Physical and functional characteristics of foam concrete: a review, Constr. Build. Mater. 221 (2019) 787–799.

[3] Z. Ge, H. Yuan, R. Sun, H. Zhang, W. Wang, H. Qi, Use of green calcium sulphoaluminate cement to prepare foamed concrete for road embankment: a feasibility study, Constr. Build. Mater. 237 (2020) 117791.

[4] K. Wu, Z. Shao, S. Qin, A solution for squeezing deformation control in tunnels using foamed concrete: a review, Constr. Build. Mater. 257 (2020) 119539.

[5] S. Ma, W. Chen, W. Zhao, Mechanical properties and associated seismic isolation effects of foamed concrete layer in rock tunnel, J. Rock Mech. Geotechnol. Eng. 11 (1) (2019) 159–171.

[6] H. Zhou, X. Zhang, X. Wang, H. Zhang, T. Song, Improving energy absorption capacity of foam concrete with gradient and layered architecture, Constr. Build. Mater. 319 (2022) 126140.

[7] P.J. Tikalsky, J. Pospisil, W. MacDonald, A method for assessment of the freeze–thaw resistance of preformed foam cellular concrete, Cem Concr Res. 34 (5) (2004) 889–893.

[8] M.H. Thakrele, Experimental study on foam concrete, Int. J. Civ. Struct. Environ. Infrastruct. Eng. Res. Dev. 4 (1) (2014) 145–158.

[9] D. Falliano, D.D. Domenico, G. Ricciardi, E. Gugliandolo, Experimental investigation on the compressive strength of foamed concrete: effect of curing conditions, cement type, foaming agent and dry density, Constr. Build. Mater. 165 (2018) 735–749.

[10] E.K.K. Nambiar, K. Ramamurthy, Models relating mixture composition to the density and strength of foam concrete using response surface methodology, Cem. Concr. Compos. 28 (9) (2006) 752–760.

[11] M. Li, H. Tan, X. He, S. Jian, G. Li, J. Zhang, X. Deng, X. Lin, Enhancement in compressive strength of foamed concrete by ultra-fine slag, Cem. Concr. Compos. 138 (2023) 104954.

[12] M. Reisi, Microstructure and mixture proportioning of non-structural foamed concrete with silica fume, Mag. Concr. Res. 69 (23) (2017) 1218–1230.

[13] Y. Guo, X. Chen, B. Chen, R. Wen, P. Wu, Analysis of foamed concrete pore structure of railway roadbed based on X-ray computed tomography, Constr. Build. Mater. 121773 (2021).

[14] Y. Zhang, Y. Jiang, T.-C. Ling, Use of CO_2 as a controlled foam stabilizer to enhance pore structure and properties of foamed concrete, Cem. Concr. Compos. 145 (2024) 105356.

[15] E.K.K. Nambiar, K. Ramamurthy, Air-void characterisation of foam concrete, Cem Concr Res. 37 (2) (2007) 221–230.

[16] W. She, Y. Du, C. Miao, J. Liu, G. Zhao, J. Jiang, Y. Zhang, Application of organic- and nanoparticle-modified foams in foamed concrete: reinforcement and stabilization mechanisms, Cem Concr Res. 106 (2018) 12–22.

[17] W. Weibull, The phenomenon of rupture in solids, Proc R Sweden Inst Eng Res 153 (1939) 1–55.

[18] W. Weibull, A statistical distribution function of wide applicability, J. Appl. Mech. 18 (3) (1951) 293–297.

[19] A. Carpinteri, G. Ferro, Size effects on tensile fracture properties: a unified explanation based on disorder and fractality of concrete microstructure, Mater. Struct. 27 (10) (1994) 563–571.

[20] A. Carpinteri, B. Chiaia, Multifractal scaling laws in the breaking behaviour of disordered materials, Chaos, Solit and Fractals. 8 (2) (1997) 135–150.

[21] A. Carpinteri, B. Chiaia, G. Ferro, Structures, size effects on nominal tensile strength of concrete structures: multifractality of material ligaments and dimensional transition from order to disorder, Mater. Struct. 28 (6) (1995) 311–317.

[22] Z.P. Bažant, Size effect in blunt fracture: concrete, rock, metal, J. Eng. Mech. 110 (4) (1984) 518–535.

[23] Z.P. Bažant, Fracture and size effect in concrete and other quasibrittle materials, CRC Press, 1998.

[24] Z.P. Bažant, M. Vořechovský, D. Novák, Asymptotic prediction of energetic-statistical size effect from deterministic finite-element solutions, J. Eng Mech. 133 (2) (2007) 153–162.

[25] X. Hu, F. Wittmann, Size effect on toughness induced by crack close to free surface, Eng. Fract. Mech. 65 (2) (2000) 209–221.

[26] K. Duan, X. Hu, F. Wittmann, Explanation of size effect in concrete fracture using non-uniform energy distribution, Mater. Struct. 35 (6) (2002) 326–331.

[27] Z.P. Bažant, B.H. Oh, Crack band theory for fracture of concrete, Mat Constr (RILEM) 16 (3) (1983) 155–177.

[28] A. Hillerborg, M. Modéer, P.-E. Petersson, Analysis of crack formation and crack growth in concrete by means of fracture mechanics and finite elements, Cem. Concr. Res. 6 (6) (1976) 773–781.

[29] Y. Jenq, S.P. Shah, Two parameter fracture model for concrete, J. Eng Mech. 111 (10) (1985) 1227–1241.

[30] S. Xu, X. Zhang, Determination of fracture parameters for crack propagation in concrete using an energy approach, Eng. Fract. Mech. 75 (15) (2008) 4292–4308.

[31] X. Hu, K. Duan, Size effect: influence of proximity of fracture process zone to specimen boundary, Eng. Fract. Mech. 74 (7) (2007) 1093–1100.

[32] X. Hu, K. Duan, Size effect and quasi-brittle fracture: the role of FPZ, Int. J. Fract. 154 (1–2) (2008) 3–14.

[33] L. Jin, W. Yu, X. Du, W. Yang, Mesoscopic numerical simulation of dynamic size effect on the splitting-tensile strength of concrete, Eng. Fract. Mech. 209 (2019) 317–332.

[34] H. Zhang, B. Šavija, Y. Xu, E. Schlangen, Size effect on splitting strength of hardened cement paste: Experimental and numerical study, Cem. Concr. Compos. 94 (2018) 264–276.

[35] D.-C. Feng, J.-Y. Wu, Phase-field regularized cohesive zone model (CZM) and size effect of concrete, Eng. Fract. Mech. 197 (2018) 66–79.

[36] Z.P. Bažant, S.D. Pang, M. Vořechovský, D. Novák, Energetic–statistical size effect simulated by SFEM with stratified sampling and crack band model, Int. J. Numer. Methods Engrg. 71 (11) (2007) 1297–1320.

[37] S.Y. Alam, P. Kotronis, A. Loukili, Crack propagation and size effect in concrete using a non-local damage model, Eng. Fract. Mech. 109 (2013) 246–261.

[38] I. Marzec, J. Tejchman, Z. Mróz, Numerical analysis of size effect in RC beams scaled along height or length using elasto-plastic-damage model enhanced by non-local softening, Finite Elem. Anal. Des. 157 (2019) 1–20.

[39] S. Sinaie, Application of the discrete element method for the simulation of size effects in concrete samples, Int. J. Solids Struct. 108 (2017) 244–253.

[40] Z. Qian, Multiscale modeling of fracture processes in cementitious materials, Technische Universiteit Delft, 2012. Ph.D Thesis).

[41] B. Lu, S. Torquato, Lineal-path function for random heterogeneous materials, Phys. Rev. A 45 (2) (1992) 922.

[42] T.-S. Han, X. Zhang, J.-S. Kim, S.-Y. Chung, J.-H. Lim, C. Linder, Area of lineal-path function for describing the pore microstructures of cement paste and their relations to the mechanical properties simulated from μ-CT microstructures, Cem. Concr. Compos. 89 (2018) 1–17.

[43] C. Yeong, S. Torquato, Reconstructing random media, Phys. Rev. E. 57 (1) (1998) 495–506.

[44] N. Jiang, Z. Ge, Y. Guan, Z. Zuo, H. Zhang, Y. Ling, B. Šavija, Experimentally validated meso-scale fracture modelling of foamed concrete, Theor. Appl. Fract. Mech. 122 (2022) 103631.

[45] J. Del Viso, J. Carmona, G. Ruiz, Shape and size effects on the compressive strength of high-strength concrete, Cem Concr Res. 38 (3) (2008) 386–395.

[46] M. Li, H. Hao, Y. Shi, Y. Hao, Specimen shape and size effects on the concrete compressive strength under static and dynamic tests, Constr. Build. Mater. 161 (2018) 84–93.

[47] N. Bossa, P. Chaurand, J. Vicente, D. Borschneck, C. Levard, O. Aguerre-Chariol, J. Rose, Micro- and nano-X-ray computed-tomography: a step forward in the characterization of the pore network of a leached cement paste, Cem Concr Res. 67 (2015) 138–147.

[48] J.-S. Kim, S.-Y. Chung, T.-S. Han, D. Stephan, M. Abd Elrahman, Correlation between microstructural characteristics from micro-CT of foamed concrete and mechanical behaviors evaluated by experiments and simulations, Cem. Concr. Compos. 112 (2020) 103657.

[49] G. Zickert, C.E. Yarman, Gaussian mixture model decomposition of multivariate signals, Signal Image Video P. 16(2) (2022) 429-436.

[50] H. Dong, P. Gao, G. Ye, Characterization and comparison of capillary pore structures of digital cement pastes, Mater Struct. 50 (2017) 1–12.

[51] L. Breiman, Random forests, Mach Learn. 45 (2001) 5–32.

[52] A. Liaw, M. Wiener, Classification and regression by randomForest, R. News. 2 (3) (2002) 18–22.

[53] U. Grömping, Variable importance assessment in regression: linear regression versus random forest, Am Stat. 63 (4) (2009) 308–319.

[54] P. Probst, M.N. Wright, A.L. Boulesteix, Hyperparameters and tuning strategies for random forest, Wiley interdiscip, Rev. Data Min. Knowl. Discov. 9 (3) (2019).

[55] P. Schratz, J. Muenchow, E. Iturritxa, J. Richter, A. Brenning, Hyperparameter tuning and performance assessment of statistical and machine-learning algorithms using spatial data, Ecol. Model. 406 (2019) 109–120.

[56] A. Delaplace, G. Pijaudier-Cabot, S. Roux, Progressive damage in discrete models and consequences on continuum modelling, J. Mech. Phys. Solids. 44 (1) (1996) 99–136.

[57] G. Lilliu, J. Van Mier, 3D lattice type fracture model for concrete, Eng. Fract. Mech. 70 (7) (2003) 927–941.

[58] J. Van Mier, M. Van Vliet, Influence of microstructure of concrete on size/scale effects in tensile fracture, Eng. Fract. Mech. 70 (16) (2003) 2281–2306.

[59] H.-K. Man, J. Van Mier, Damage distribution and size effect in numerical concrete from lattice analyses, Cem. Concr. Compos. 33 (9) (2011) 867–880.

[60] E. Schlangen, Fracture simulations of concrete using lattice models: computational aspects, Eng. Fract. Mech. 57 (2) (1997) 319–332.

[61] M. Yip, J. Mohle, J. Bolander, Automated modeling of three-dimensional structural components using irregular lattices, Comput-Aided Civ Inf. 20 (6) (2005) 393–407.

[62] H. Zhang, B. Šavija, E. Schlangen, Towards understanding stochastic fracture performance of cement paste at micro length scale based on numerical simulation, Constr. Build. Mater. 183 (2018) 189–201.

[63] H. Zhang, B. Šavija, S. Chaves Figueiredo, M. Lukovic, E. Schlangen, Microscale testing and modelling of cement paste as basis for multi-scale modelling, Mater. 9 (11) (2016) 907.

[64] H. Zhang, B. Šavija, E. Schlangen, Combined experimental and numerical study on micro-cube indentation splitting test of cement paste, Eng. Fract. Mech. 199 (2018) 773–786.

[65] H. Zhang, Y. Xu, Y. Gan, E. Schlangen, B. Šavija, Experimentally validated meso-scale fracture modelling of mortar using output from micromechanical models, Cem. Concr. Compos. 110 (2020) 103567.

[66] G. Lilliu, 3D analysis of fracture processes in concrete, Delft University of Technology, Delft, The Netherlands, 2007. PhD. Thesis.

[67] N. Jiang, H. Zhang, Z. Chang, E. Schlangen, Z. Ge, B. Šavija, Discrete lattice fracture modelling of hydrated cement paste under uniaxial compression at micro-scale, Constr. Build. Mater. 263 (2020) 120153.

[68] M.R.A. van Vliet, J.G. van Mier, Experimental investigation of concrete fracture under uniaxial compression, Mech Cohes-Frictional Mater. 1 (1) (1996) 115–127.
[69] H. Chandler, I. Merchant, R. Henderson, D. Macphee, Enhanced crack-bridging by unbonded inclusions in a brittle matrix, J. Eur. Ceram. Soc. 22 (1) (2002) 129–134.
[70] D. Liu, B. Šavija, G.E. Smith, P.E. Flewitt, T. Lowe, E. Schlangen, Towards understanding the influence of porosity on mechanical and fracture behaviour of quasi-brittle materials: experiments and modelling, Int. J. Fract. 205 (2017) 57–72.
[71] J. Van Mier, S. Shah, M. Arnaud, J. Balayssac, A. Bascoul, S. Choi, D. Dasenbrock, G. Ferrara, C. French, M. Gobbi, Structures, strain-softening of concrete in uniaxial compression: report of the round Robin test carried out by RILEM TC 148-SSC, Mater. Struct. 30 (1997) 195–209.
[72] D. Falliano, D.D. Domenico, A. Sciarrone, G. Ricciardi, L. Restuccia, J. Tulliani, E. Gugliandolo, Fracture behavior of lightweight foamed concrete: the crucial role of curing conditions, Theor. Appl. Fract. Mech. 103 (2019) 102297.
[73] T.T. Nguyen, H.H. Bui, T.D. Ngo, G.D. Nguyen, Experimental and numerical investigation of influence of air-voids on the compressive behaviour of foamed concrete, Mater Design 130 (2017) 103–119.
[74] J. Dang, S. Zhao, G. Chen, X. Cao, J. Yang, Effect of polyethylene powder and heating treatment on the microstructure and hardened properties of foam concrete, J Build Eng 50 (2022) 104143.
[75] E.M. Golafshani, A. Behnood, M. Arashpour, Predicting the compressive strength of normal and high-performance concretes using ANN and ANFIS hybridized with Grey wolf optimizer, Constr. Build. Mater. 232 (2020) 117266.
[76] J.J.J. Moré, D.C. Sorensen, Computing a trust region step, SIAM J. Sci.stat Comput. 4 (3) (1983) 553–572.
[77] C.-C. Vu, N.-K. Ho, T.-A. Pham, Weibull statistical analysis and experimental investigation of size effects on the compressive strength of concrete-building materials, Case Stud Constr Mat. 17 (2022).
[78] A. Carpinteri, Scaling laws and renormalization groups for strength and toughness of disordered materials, Int. J. Solids Struct. 31 (3) (1994) 291–302.